Journal of Materials Chemistry A

ROYAL SOCIETY OF CHEMISTRY

PAPER

View Article Online
View Journal | View Issue

Cite this: J. Mater. Chem. A, 2026, 14, 12415

Luminescent Zr(IV) metal–organic frameworks as sensors of waterborne persistent organic pollutants: reproducibility and transferability

Anna Mauri, [a] Gioele Colombo [a] and Simona Galli *[ab]

Metal–organic frameworks (MOFs) have shown great potentiality as chemical sensors of waterborne persistent organic pollutants (POPs). To emphasise the relevance, in this applicative context, of statistically grounded protocols ensuring results reproducibility, reliability and comparability, we investigated the two polymorphic MOFs NU-1000 and NU-901 as luminescent sensors of four exemplary waterborne pharmaceuticals: diclofenac sodium (DCF), fluoxetine hydrochloride, paracetamol (PAR) and acetylsalicylic acid. In POP distilled water solutions 0.3–9.5 μM, NU-1000 exhibited a reproducible behaviour irrespective of the pollutant. Nonetheless, its response was distinguishable from that due to its simple dilution, *i.e.* it was genuinely due to the POP, only with DCF. Toward the latter, NU-1000 showed a reproducible performance even across aqueous matrices of higher complexity – bottled and tap water – and under two different experimental protocols, with binding constants and limits of detection, respectively, on the order of 10^5 M^{-1} (namely: 2.4(1) × 10^5 M^{-1} in distilled water, and 2.1(7) × 10^5 M^{-1} averaged over the three matrices) and 10^{-1} μM (0.7(2) μM averaged over the three matrices). In similar experimental conditions, NU-901 showed reproducibility only with DCF and PAR, with a non-monotonic trend due to the alternative prevalence, on the sensor signal, of MOF/POP interactions or MOF dilution. Overall, this case study successfully emphasises the importance of crucial features – statistically validated reproducibility of sensor performance and operative conditions, such as sensor dilution, complexity of the working matrix – thus concurring to advance best practices in the field and providing a basis upon which improved porous material-based sensing systems can be engineered and tested.

Received 2nd January 2026
Accepted 13th February 2026

DOI: 10.1039/d6ta00023a

rsc.li/materials-a

1. Introduction

Persistent organic pollutants (POPs) are a steadily growing class of organic compounds of anthropic origin that resist environmental degradation and, consequently, pose significant risks to both ecological systems and human health.[1–5] This class of chemicals includes, *e.g.*, polychlorinated biphenyls,[6,7] polycyclic aromatic hydrocarbons,[8] dioxins,[9] organochlorine pesticides[10,11] and active pharmaceutical ingredients.[12] With reference to the hydrosphere, their incessant massive usage, combined to the limits of current wastewater treatment technologies, which do not efficiently remove these substances, have raised global concern. The latter is witnessed, *e.g.*, by Goal 6 ("Clean Water and Sanitation") of the 17 Sustainable Development Goals issued by the United Nations in 2015,[13] calling for action to "ensure availability and sustainable management of water and sanitation for all", and by the increasing regulatory efforts at the international[14] and European[15] levels.

Based on the above, engineering and implementation of innovative water remediation technologies remains a pressing challenge for basic and applied research in academia and industry. Parallel to this is the quest for sensitive, selective, and reliable detection methods.

Metal–organic frameworks (MOFs) are porous, crystalline materials obtained through the self-assembly of metal-containing nodes and polytopic organic linkers. Their open polymeric architectures combine high specific surface areas with well-defined and optimizable pore dimension and chemical functionality.[16] Among their numerous applicative contexts, MOFs have shown great potential in the fields of chemical sensing[17,18] and removal.[19] As luminescent sensors,[20–24] MOFs successfully translate molecular recognition events into detectable and quantifiable optical signals. This performance makes them particularly attractive for the detection of trace pollutants, that require high sensitivity and discrimination in complex matrices such as waters. MOF/POP interactions can result in observable changes in MOF photoluminescence, such as intensity quenching[25,26] or enhancement,[27,28] or maximum wavelength shift, which can be fruitfully employed as the basis for sensing. Relevant publications highlight high selectivity[29–31]

[a]Dipartimento di Scienza e Alta Tecnologia, Università degli Studi dell'Insubria, Via Valleggio 9, 22100 Como, Italy. E-mail: simona.galli@uninsubria.it
[b]Consorzio Interuniversitario Nazionale per le Scienze e Tecnologie dei Materiali (INSTM), Via Giusti 7, 50121 Firenze, Italy

and low limits of detection.[32–34] As the field moves toward more application-driven research, *e.g.* with portable sensing devices,[35,36] the implementation of evaluation strategies granting reproducibility and transferability becomes increasingly urgent.

In this context, through the present work we aim at emphasising the key role of a statistically robust protocol to evaluate the performance of luminescent MOFs as sensors for persistent organic pollutants in water matrices of different complexity, taking into due consideration typically disregarded contributions, such as that of sensor dilution.

To the aim, we selected the two renown MOFs NU-1000[37] and NU-901,[38] sharing the minimal formula $[Zr_6(\mu_3\text{-}O)_4(\mu_3\text{-}OH)_4(\mu\text{-}OH)_4(H_2O)_4(TBAPy)_2]$ and possessing linker-based luminescence. Zr-based MOFs, for example those belonging to the "NU" family (NU = Northwestern University), have shown exceptional thermal and chemical stability, as well as good stability in aqueous environments.[39] The micro/mesoporous MOF NU-1000 was selected as it shows a consolidated synthesis, also scalable to the gram-level,[40] as well as a solid analytical and structural characterization, and has already been successfully employed as sensor for various analytes.[41–43] Though less investigated than NU-1000, NU-901 was chosen as a purely microporous counterpart already tested as sensor for polyaromatic hydrocarbons[43] and volatile organic compounds.[44] In the present work, we employed the two MOFs as sensors of four active pharmaceutical ingredients [diclofenac sodium (DCF), fluoxetine hydrochloride (FXT), paracetamol (PAR) and acetylsalicylic acid (ACA); Scheme 1] as exemplary POPs. These POPs, sharing similar molecular structures with only fully carbocyclic aromatic rings, were selected to explore the influence of different functional groups (carboxylates, amines, amides, esters) and electric charges on the MOFs sensing performances. Additionally, DCF, PAR and ACA are among the ten most consumed drugs in Italy and Europe.[45] This occurrence is reflected in their reported concentrations in European waters (up to 5.3 μg L^{-1} for DCF,[46] 34 μg L^{-1} for PAR[47] and 80.4 μg L^{-1} for ACA[48]). On the other hand, FXT was proposed to be included in the 5th European Watchlist under the Water Framework Directive,[49] having been detected in concentrations as high as 0.596 μg L^{-1}.[50]

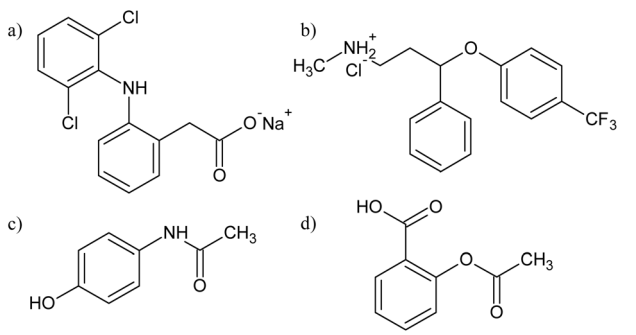

Scheme 1 Molecular structure of the POPs exploited in this work: (a) diclofenac sodium (DCF), (b) fluoxetine hydrochloride (FXT), (c) paracetamol (PAR) and (d) acetylsalicylic acid (ACA).

Employing different experimental protocols and water matrices – distilled, bottled and tap water – we show how a statistics-driven workflow can reveal reliable and reproducible sensor responses, discriminate between genuine analyte-induced response and background variability and, ultimately, improve the reliability of MOF-based sensing systems. Hence, this study case not only concurs to advance best practices in the field but also provides a foundational basis upon which future sensing tests can be built with greater consistency.

2. Experimental section

2.1. Materials and methods

All the solvents and reagents used for the syntheses and manipulations hereby described were purchased from commercial vendors and were used without further purification. *N*,*N*-Dimethylformamide (>98%) was purchased from Carlo Erba; fluoxetine hydrochloride (>98%), diclofenac sodium (>98%) and paracetamol (>98%) were purchased from TCI Chemicals; benzoic acid (>99.5%), zirconyl chloride octahydrate (>98%) and acetylsalicylic acid (>99%) were purchased from Sigma Aldrich; 1,3,6,8-tetrakis(4-*p*-benzoic acid)pyrene (>97%) was purchased from BLDpharm. Elemental composition analyses (C, H, N% wt.) were performed with a PerkinElmer 2400 Series II CHN Analyser. Thermogravimetric analyses (TGAs) and differential scanning calorimetry (DSC) analyses were carried out simultaneously with a Netzsch STA 409 PC Luxx instrument on powdered samples (*ca.* 10 mg) of thermally activated NU-1000 and NU-901, working under a synthetic air flow ($N_2 : O_2 = 80 : 20$; flow rate = 40 mL min^{-1}) in the temperature range 293–1173 K and with a heating rate of 5 K min^{-1}. For details on the thermal activation procedure, the reader is addressed to Sections 2.2 and 2.3 for NU-1000 and NU-901, respectively. X-ray fluorescence (XRF) elemental analyses were performed in air under ambient conditions on powdered samples (*ca.* 5 mg) of thermally activated NU-1000 and NU-901 using a PANalytical MINIPAL 2 instrument equipped with a sealed X-ray tube having a Cr anode. The spectrometer generator was set at 30 kV and 3 μA. ^{1}H-NMR spectra were recorded at 400 MHz with a Bruker AVANCE 400 spectrometer on digested samples of the two MOFs: after thermal activation, a powdered sample of the MOF (*ca.* 1 mg) was dissolved in 96–98% deuterated sulphuric acid (5 drops), and the obtained solution was sonicated in an ultrasound bath for 5 min. The red oil thus formed was dissolved in deuterated dimethyl sulfoxide. In the following, the chemical shift (δ) values are reported in ppm relative to residual solvent signals as internal reference and are labelled as: s = singlet, d = doublet, m = multiplet. Infrared (IR) spectra were acquired in the attenuated total reflectance mode over the range 4000–600 cm^{-1} with a Nicolet iS10 instrument. In the following and the SI, the IR bands are reported in cm^{-1} and are labelled as: s = strong; m = medium; w = weak; vb = very broad; sh = sharp. Powder X-ray diffraction (PXRD) patterns were acquired using a Bruker AXS D8 Advance vertical-scan $\theta : \theta$ diffractometer equipped with a sealed X-ray tube (Cu K_α, λ = 1.5418 Å), a Bruker Lynxeye linear position-sensitive detector, a filter of nickel in the diffracted beam,

primary- and secondary-beam Soller slits (aperture: 2.5°), a fixed divergence slit (aperture: 0.5°), an anti-scatter slit (aperture: 8 mm). The diffractometer generator was set at 40 kV and 40 mA. After thermal activation, powdered samples of NU-1000 or NU-901 (*ca.* 20 mg) were deposited into the cavity of a silicon free-background sample-holder 0.2 mm deep. For qualitative analyses, PXRD patterns were typically acquired in the 2θ range 2.0–35.0°. The acquisitions were followed by whole powder pattern refinements with the Le Bail approach[51] using the software TOPAS-R v.3.[52] The already published structural information of NU-1000[37] and NU-901[53] was used as starting point.

2.2. Synthesis of NU-1000

NU-1000 was synthesized in the form of microcrystalline powders according to an already reported procedure:[54] in a glass vial, zirconyl chloride octahydrate ($ZrOCl_2 \cdot 8H_2O$, 97 mg, 0.3 mmol) and benzoic acid (2.7 g, 22 mmol) were dissolved in anhydrous dimethylformamide (DMF, 8 mL) *via* sonication in an ultrasound bath. The obtained colourless solution was heated in an oven at 353 K for 1 h. After this time lapse, the vial was cooled down to room temperature. 1,3,6,8-Tetrakis(4-*p*-benzoic acid)pyrene (H_4TBAPy, 40 mg, 0.06 mmol) was then added into the vial. The obtained suspension was sonicated until it became visually homogeneous. The vial was then heated in an oven at 373 K for 24 h. After this time lapse, the yellow powder present at the bottom of the vial was recovered by centrifugation (7000 rpm, 5 min) and was washed with DMF (3 × 10 mL) under magnetic stirring over the course of 24 h. After washing, the solid was suspended in fresh DMF (12 mL), and aqueous HCl 8 M (0.5 mL) was added. The obtained suspension was heated in an oven at 373 K for 18 h. Then, the vial was cooled down to room temperature, and the solid was recovered by centrifugation (7000 rpm, 5 min) and was washed with DMF (3 × 10 mL) under magnetic stirring over the course of 24 h. Finally, solvent exchange was performed to facilitate thermal activation: after the removal of the last aliquot of DMF, the solid was washed with acetone (3 × 10 mL) under magnetic stirring over the course of 24 h, followed by heating of the recovered powder at 393 K under vacuum for 12 h. Yield: 50 mg (76% m/m *vs.* H_4TBAPy). ^{1}H-NMR (DMSO-d_6, δ, ppm) (Fig. S1a): 7.76 (d), 7.96 (s), 8.09–8.06 (m) (the reader is addressed to the inset of Fig. S1a for the attribution of the signals). IR (neat, cm^{-1}) (Fig. S2b): 3384, m, vb, ν(OH); 1600, 1412, s, sh, symmetric and asymmetric ν(C=O); 1181, w, sh; 784, 712, w, sh, Zr–O vibrations[55] (the reader is addressed to Fig. S2a for a comparison with the IR spectrum of H_4TBAPy). Elemental analysis: calculated for the minimal formula $Zr_6O_4(OH)_8(H_2O)_4(TBAPy)_2 \cdot 6.5H_2O$ (hydration deriving from sample manipulation at ambient conditions after thermal activation): C = 46.08%, H = 3.21%; found C = 45.76%, H = 2.95%.

2.3. Synthesis of NU-901

NU-901 was synthesized according to an already reported procedure:[44] in a glass vial, $ZrOCl_2 \cdot 8H_2O$ (32 mg, 0.1 mmol) and benzoic acid (61 mg, 0.5 mmol) were dissolved in anhydrous DMF (1 mL) *via* sonication in an ultrasound bath. Then, H_4TBAPy (34 mg, 0.05 mmol) and aqueous HCl 37% m/m (25 μL) were added. The obtained suspension was sonicated in an ultrasound bath until it became visually homogeneous. Then, it was heated in an oven at 373 K for 24 h. A yellow gel was obtained, transferred into a plastic vial, and washed with DMF (10 mL) under magnetic stirring for 24 h. After this time lapse, a yellow powder was obtained, recovered by centrifugation (7000 rpm, 5 min), and washed with the same procedure two more times. After the removal of the last aliquot of DMF, ethanol (10 mL) was added, and the suspension was kept under magnetic stirring for 24 hours, followed by the recovery of the solid by centrifugation (7000 rpm, 5 min). This washing procedure was repeated two more times. After the removal of the last aliquot of ethanol, the powder was recovered by centrifugation (7000 rpm, 5 min) and was heated at 393 K under vacuum for 12 h. Yield: 30 mg (88% m/m *vs.* $ZrOCl_2 \cdot 8H_2O$). ^{1}H-NMR (DMSO-d_6, δ, ppm) (Fig. S1b): 7.75 (d), 7.95 (s), 8.05–8.08 (m) (the reader is addressed to the inset of Fig. S1b for the attribution of the signals). IR (neat, cm^{-1}) (Fig. S2c): 3380, m, vb, ν(OH); 1599, 1410, s, sh, symmetric and asymmetric ν(C=O); 1182, w, sh; 785, 716, w, sh, Zr–O vibrations[55] (the reader is addressed to Fig. S2a for a comparison with the IR spectrum of H_4TBAPy).

2.4. Thermal stability evaluation

To complement the results of simultaneous TGA and DSC, the thermal behaviour of NU-1000 was studied *in situ* by temperature-resolved powder X-ray diffraction (TR-PXRD) using the diffractometer described in Section 2.1. To the aim, a powdered sample of NU-1000 (*ca.* 10 mg), thermally activated as described in Section 2.2, was placed in the cavity of an aluminium sample holder and was heated in air using a custom-made heater (Officina Elettrotecnica di Tenno, Ponte Arche, Italy). The experiment was carried out in the temperature range 298–758 K, making steps of 20 K and acquiring a PXRD pattern at each step in isothermal conditions in the 2θ range 2.0–20.0°, with steps of 0.02° and a time per step of 1 s. A parametric whole powder pattern refinement with the Le Bail approach was subsequently performed. To the aim, the data were divided into two sets (318–538 K and 538–658 K) according to their slope, as observed through a preliminary pattern-by-pattern refinement. For the data acquired above 658 K, the crystallinity degree of the sample, hence the data quality, was too limited to encourage any data treatment.

2.5. Water stability assessment

NU-1000 and NU-901 water stability was monitored by powder X-ray diffraction: a powder pattern of a sample of MOF (*ca.* 2 mg), preliminarily activated as described in Sections 2.2 and 2.3, was acquired as zero-point. Then, the sample was suspended in distilled water (2 mL) and kept under magnetic stirring for different time lapses (2, 4, and 6 h). After each time lapse, the suspension was centrifuged (10 000 rpm, 5 min) and the solid was recovered and dried under a flow of N_2. A PXRD pattern was then acquired. In the case of NU-1000, the patterns

were acquired with the diffractometer described in Section 2.1, working in the 2θ range 2.0–35.0°, with steps of 0.02° and a time per step of 1 s. As for NU-901, the patterns were acquired using a Rigaku Miniflex 300 vertical-scan $\theta:2\theta$ diffractometer equipped with a sealed X-ray tube (Cu K_α, $\lambda = 1.5418$ Å), a filter of nickel in the diffracted beam, a Rigaku D/teX Ultra linear position-sensitive detector, primary- and secondary-beam Soller slits (aperture: 2.5°), a variable divergence slit, an anti-scatter slit (aperture: 8 mm). The generator was set at 30 kV and 10 mA.

2.6. Optical spectroscopy properties evaluation in distilled water

The electronic absorption and fluorescence emission spectra were recorded on an Edinburgh Instruments FS5 fluorescence spectrometer equipped with a 150 W continuous xenon lamp as light source and an additional detector for transmittance. The equipment was controlled through the Fluoracle® software package (V. 1.9.1). Hellma Analytics fluorometric 1 cm-path quartz cuvettes were used as sample holders. The acquired data were corrected for the instrument wavelength response. To evaluate the spectroscopic properties of H_4TBAPy in the same environment of the title applicative context, a 50 μM distilled water suspension of the compound was prepared and kept under magnetic stirring till the acquisition of the electronic absorption and fluorescence emission spectra. To assess the spectroscopic properties of thermally activated samples of NU-1000 and NU-901, a suspension was prepared introducing a powdered batch of MOF (*ca.* 5 mg) in distilled water (50 mL) and was kept under vigorous magnetic stirring for 2 h. An aliquot (2 mL) of the suspension was then transferred into a cuvette and was immediately analysed. The electronic absorption spectra were recorded in the range 200–700 nm. The maximum absorption wavelength thus determined ($\lambda_{abs,max}$ = 433, 411 and 435 nm for H_4TBAPy, NU-1000 and NU-901, respectively) was used as excitation wavelength (λ_{ex}) to record the fluorescence emission spectra. Finally, the electronic absorption spectra of 50 μM distilled water solutions of the selected POPs (DCF, PAR, FXT or ACA; Scheme 1) were recorded to independently confirm that they do not absorb electromagnetic radiation in the spectral range used for the sensing experiments.

2.7. Pollutants sensing in distilled water: experimental protocol, statistical analysis and mathematical modelling

The sensing ability of NU-1000 and NU-901 toward the selected POPs was first evaluated using distilled water as aqueous matrix for both MOF and POP. An aqueous suspension of each MOF with concentration of *ca.* 100 mg L^{-1} was prepared and was kept under magnetic stirring till its usage. An aliquot (2 mL) of the suspension was introduced in a cuvette, and a fluorescence emission spectrum was recorded as zero point with the instrument and λ_{ex} quoted in Section 2.6. To improve the signal-to-noise ratio, for each datapoint of the experiments described in this section and in Section 2.8, two emission spectra were acquired one after the other and were summed. To figure out the contribution of MOF dilution to its fluorescence emission spectrum, subsequent aliquots of distilled water were added to the MOF suspension in the cuvette, gently shaking the latter till the suspension appeared homogeneous at the naked eye and acquiring a fluorescence emission spectrum after each addition. For both MOFs, dilution provoked fluorescence quenching without any variation of the emission maximum or spectrum overall shape. The behaviour of the absolute or relative emission intensity variation [ΔI or ΔI(%), respectively] as a function of MOF concentration was modelled using an exponential function with the software MATLAB.[56] The resulting equation was subsequently used to describe the contribution of dilution to the emission intensity of the MOF at comparison to that of the POPs.

According to what will be addressed as Protocol 1 in the following, 46–48 μM stock aqueous solutions of the selected POPs were prepared. For each POP, a fresh aqueous suspension of MOF with concentration of *ca.* 100 mg L^{-1} was prepared and was kept under magnetic stirring until it was used. An aliquot (2 mL) of the suspension was introduced in a cuvette. Then, after a zero-point acquisition, aliquots of POP aqueous solutions were subsequently added to the MOF suspension. After each addition, the cuvette was gently shacked till the suspension appeared homogeneous at the naked eye, and an emission spectrum was acquired. Changes in the emission spectra with respect to the zero-point were monitored. The volume of POPs solution aliquots added to the 2 mL MOF suspension differed from one POP to the other (see Table S1 for the actual values) to grant the investigation of the same POP molar concentration ([POP]) at any point. All the measurements were performed in triplicate, spanning the same [POP] range with three fresh MOF suspensions and POP solutions. For each test involving NU-1000, since we did not observe a significant variation in the position of the emission maximum ($\Delta\lambda_{fluo,max} \leq 5$ nm), we calculated the absolute variation of the emission intensity, ΔI, using the intensity values at the maximum ($\lambda_{fluo,max}$) of the zero-point measurement according to eqn (1):

$$\Delta I = I_x - I_0 \quad (1)$$

where I_x and I_0 are the maximum intensity at a given POP concentration and at the zero-point, respectively. In the case of NU-901, for the experiments with FXT and ACA ΔI was calculated as described for NU-1000. Conversely, since with PAR and DCF ΔI was accompanied by a $\lambda_{fluo,max}$ shift of *ca.* 10 nm ΔI was calculated estimating I_x at the actual $\lambda_{fluo,max}$.

For NU-1000, a statistical analysis was carried out employing the values of ΔI at [POP] = 6.3 μM (selected as exemplary [POP] value). Single Factor Analysis of Variance (ANOVA) and Tukey's Honest Significant Difference test[57] were recurred to.

Based on the outcomes of the statistical analysis, the average values of ΔI obtained with DCF were modelled as a function of [DCF] through a binding function[58] (eqn (2)):

$$\Delta I = \frac{\Delta I_{max} K\alpha[POP]}{1 + K\alpha[POP]} \quad (2)$$

where $\Delta I_{max} = I_\infty - I_0$, I_0 is the MOF emission intensity in the absence of POP, I_∞ is the emission intensity for a complete MOF/POP interaction and K_α is the binding constant. To

estimate the limit of detection (LoD), we considered the [POP] range in which the average ΔI could be interpolated with a straight line according to the equation:

$$\Delta I = m \times [\mathrm{POP}] + q \quad (3)$$

and we calculated the LoD using the equation:

$$\mathrm{LoD} = \frac{3\sigma_b}{m} \quad (4)$$

where m is the slope of the straight line modelling ΔI *vs.* [POP] (eqn (3)) and σ_b is the standard deviation of the blank measurement. As no standard deviation was available for ΔI at [POP] = 0 M, we considered as standard deviation the error calculated for the intercept q of eqn (3) by the software MATLAB (corresponding to the 95% confidence bound).

In the case of NU-901, a statistical analysis of the MOF response in presence of DCF and PAR was performed applying the *F*-test followed by the *t*-test on the values of ΔI at [POP] = 1.45 μM (as exemplary value of [POP]).

Finally, given the behaviour of NU-901 in presence of PAR and DCF (see Section 3.7), an additional experiment was carried out at low [POP] values (0.05–1.5 μM and 0.1–1.5 μM for PAR and DCF, respectively). Since the effect of dilution would have been more evident in this concentration range, a different protocol (Protocol 2 in the following) was applied. An aqueous suspension of NU-901 with concentration of *ca.* 100 mg L^{-1} was prepared and left under magnetic stirring until its usage. Stock aqueous solutions with [POP] in the range 4.8–16.8 μM and 6.9–27.7 μM were prepared for PAR and DCF, respectively. An aliquot (2 mL) of MOF suspension was introduced in a cuvette, and its fluorescence emission spectrum was recorded as zero-point. Then, an aliquot (20 μL) of POP solution was added to the cuvette. After gently shaking the latter till the suspension appeared homogeneous at the naked eye, a fluorescence emission spectrum was acquired. ΔI was calculated according to eqn (1) using the intensities at the $\lambda_{fluo,max}$ of the zero-point. For both POPs, the variation of ΔI as a function of [POP] was modelled using a binding function (eqn (2)), and the limit of detection was estimated as explained above for NU-1000 (eqn (3) and (4)).

2.8. DCF sensing in different aqueous matrices: experimental protocol, statistical analysis and mathematical modelling

The couple NU-1000/DCF was selected to study the influence of the nature of POP aqueous matrix, namely: distilled water, bottled water and tap water. The composition of the sample of bottled water used in the present study, as reported by the vendor in the relevant tag, is reported in Table S2. The composition of the sample of tap water in the period in which it was sampled for the present study, as published by the municipal water company, is reported in Table S3. A *ca.* 100 mg L^{-1} suspension of NU-1000 in distilled water was prepared and kept under magnetic stirring till its usage. To evaluate the contribution of dilution, 2 mL of MOF suspension were placed in a quartz cuvette, and its fluorescence emission spectrum was acquired. Then, a series of fluorescence emission spectra were recorded after adding, to fresh aliquots of NU-1000 suspension in the cuvette, the same volumes of distilled water which would have been adopted for the sensing study (Table S1). The same procedure was repeated adding bottled and tap water to renewed aliquots of NU-1000 distilled water suspension.

Stock aqueous solutions of DCF 47 μM (15 mg L^{-1}) were prepared in distilled, bottled and tap water. For each matrix, after a zero-point acquisition, a series of fluorescence emission spectra were acquired at various [DCF]. The MOF suspension in the cuvette was changed at each point, followed by the addition of increasing volumes of the same DCF stock solution (Protocol 3) and cuvette shaking till the suspension appeared homogeneous at the naked eye. Changes in the emission intensity, emission maximum or spectrum overall shape were monitored. For each aqueous matrix, three replicates were performed. The resulting curves ΔI(%) *vs.* [DCF] were modelled using a binding function (eqn (2)). The limits of detection in the three matrices were calculated as described in Section 2.7.

3. Results and discussion

3.1. NU-1000 and NU-901 synthesis and preliminary characterization

Already reported procedures were adopted to prepare NU-1000[54] and NU-901[44] in the form of powders. After solvent exchange followed by thermal activation, the isolated batches were characterized by juxtaposing infrared (IR), X-ray fluorescence (XRF) and ^{1}H-NMR spectroscopy, as well as powder X-ray diffraction (PXRD). As shown by Fig. S2 and its caption, where the IR spectra of NU-1000 and NU-901 are proposed and commented at comparison with that of H_4TBAPy, IR spectroscopy preliminarily confirmed the coordination of the linker to the Zr^{IV} ions and the absence of residual solvent. ^{1}H-NMR spectroscopy on digested samples of NU-1000 and NU-901 (Fig. S1) highlighted the absence of benzoic acid (used as modulator and removed upon treatment with a $HCl_{(aq)}$/DMF mixture; see Sections 2.2 and 2.3). XRF spectroscopy (Fig. S3) excluded the presence of chlorine (in the form of chloride anions originating from HCl, potentially coordinating the metal ions and successfully removed through the final washing procedures). Finally, as assessed by PXRD, NU-1000 and NU-901 were recovered in the form of microcrystalline and nanocrystalline powders, respectively (Fig. S4). Whole powder pattern refinements performed with the Le Bail approach and employing, as starting point, the space group and unit cell parameters reported in the literature (37 and 53 for NU-1000 and NU-901, respectively) confirmed their phase purity.

3.2. NU-1000 and NU-901 structural aspects: a brief overview

For the sake of completeness, we report in the following a brief description of the crystal structure of the polymorphic MOFs NU-1000 and NU-901. Despite sharing the same $[Zr_6(\mu_3\text{-}O)_4(\mu_3\text{-}OH)_4(\mu\text{-}OH)_4(H_2O)_4(TBAPy)_2]$ minimal formula, octahedral $[Zr_6(\mu_3\text{-}O)_4(\mu_3\text{-}OH)_4(\mu\text{-}OH)_4(H_2O)_4]^{8+}$ node (Fig. 1a),[59] node connectivity, and linker coordination mode, the two MOFs

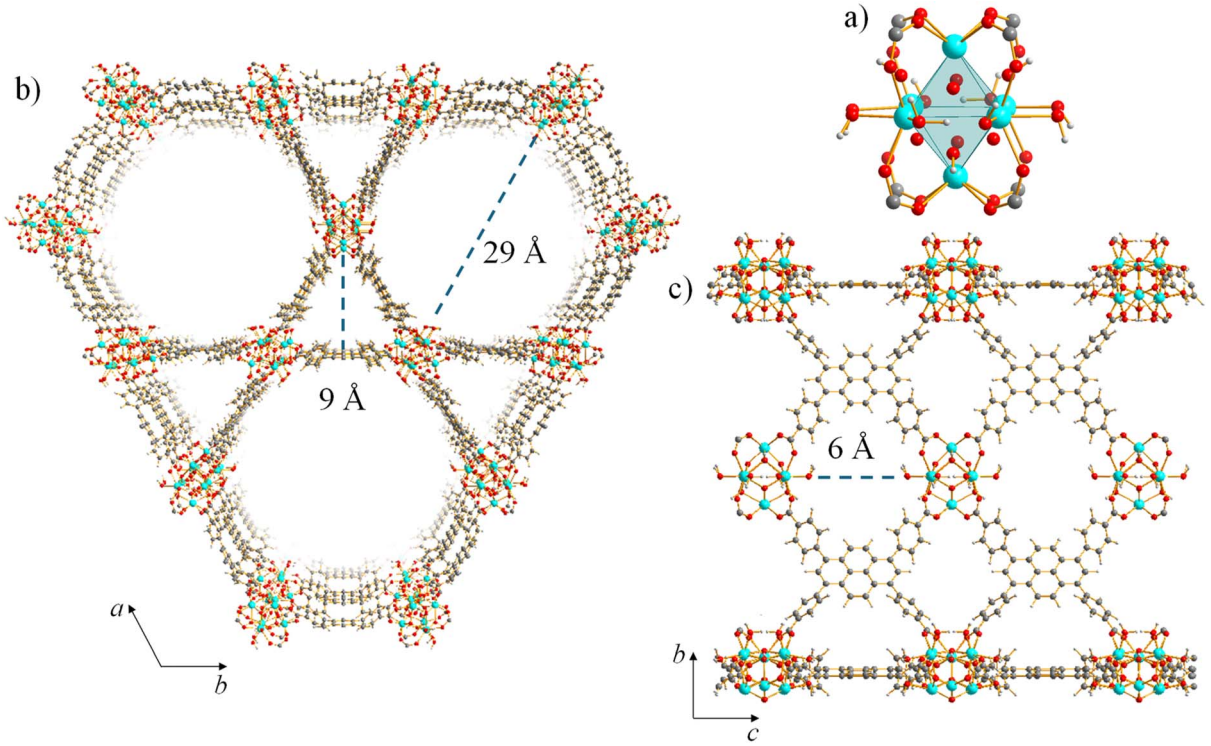

Fig. 1 Representation of the crystal structure of NU-1000: (a) the node. (b) Portion of the framework viewed approximately along the crystallographic *c*-axis; highlighted the width[60] of the microporous and mesoporous channels. (c) Portion of the framework viewed along the crystallographic *a*-axis; highlighted the width[61] of the rhombic window. Element colour code: C, dark grey; H, light grey; O, red; Zr, cyan. Crystallographic information retrieved from 37.

differ in the crystal structure and inherent porosity. NU-1000 shows a microporous/mesoporous 3-D framework with **csq** topology featuring triangular microporous and hexagonal mesoporous channels *ca.* 9 Å and 29 Å wide, respectively[60] (Fig. 1b). The lateral access to the hexagonal channels is provided by rhombic windows *ca.* 6 Å wide (Fig. 1c).[61] At variance, NU-901 is characterized by a 3-D microporous framework with **scu** topology showing rhombic channels *ca.* 9 Å wide. The lateral access to the channels is regulated by windows *ca.* 5 Å wide (Fig. 2).[62]

3.3. NU-1000 and NU-901 water and thermal stability

The collapse of the 3-D architecture of NU-1000 was previously assessed *via* PXRD and N_2 adsorption at 77 K after the

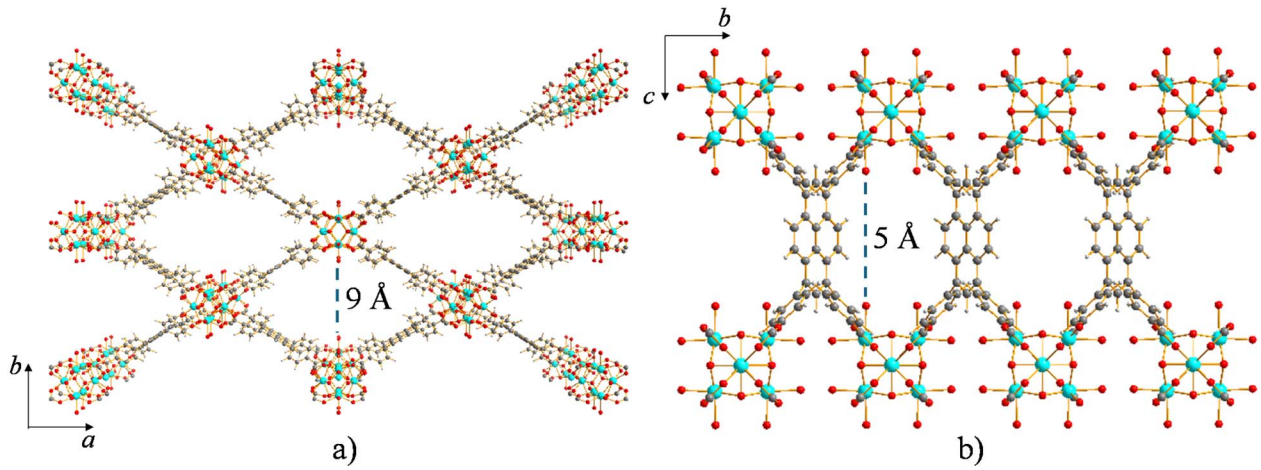

Fig. 2 Representation of the crystal structure of NU-901: (a) portion of the framework viewed approximately along the crystallographic *c*-axis; highlighted the width[62] of the rhombic microporous channels. (b) Portion of the framework viewed along the crystallographic *a*-axis; highlighted the width of the rhombic windows. Element colour code: C, dark grey; H, light grey; O, red; Zr, cyan. Crystallographic information retrieved from 53.

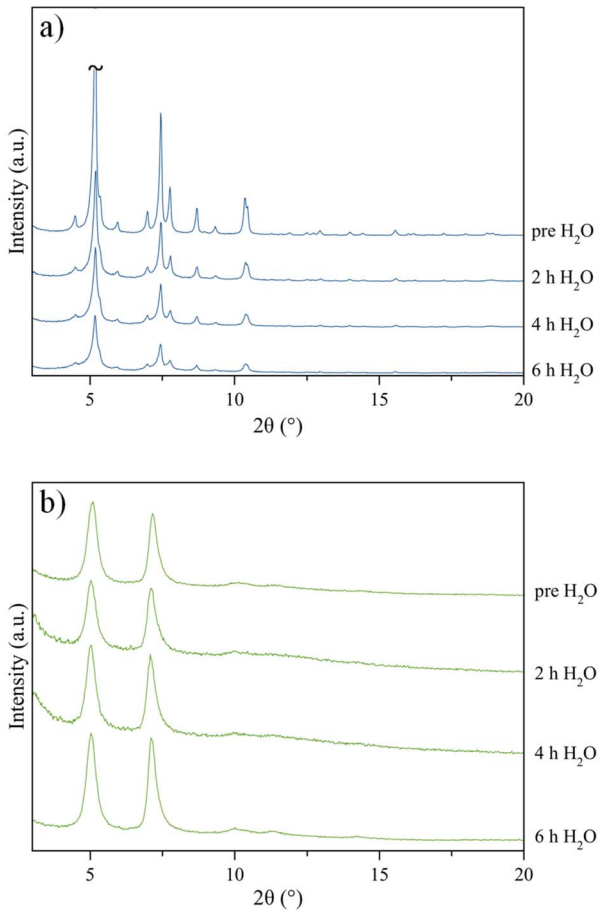

Fig. 3 PXRD patterns acquired on thermally activated (a) NU-1000 and (b) NU-901 prior to and after suspension in distilled water at ambient conditions for different time lapses.

acquisition of 1-to-3 water adsorption/desorption isotherms at 298 K. That occurrence ultimately witnessed the inefficacy of direct activation of this MOF from aqueous environments.[63] At variance, to our knowledge no information is available about the stability of NU-1000 or NU-901 in aqueous suspensions, *i.e.* in the applicative context under investigation. In the present work, the stability of thermally activated batches of the two MOFs suspended in distilled water was ascertained up to 6 h (Fig. 3), a time frame compatible with that of the sensing experiments performed according to Protocol 1 (see Section 2.7). Incidentally, as shown by Fig. 3a, in the case of NU-1000 a slight loss of crystallinity accompanies the increase of suspension time, as confirmed by a semi-quantitative estimation of the average crystal domain size performed through whole powder pattern refinements assuming a spherical morphology (Table S4). Notably, this occurrence has apparently no effect on NU-1000 sensing performances, which were found to be reproducible across experiments lasting different time lapses (see below). In the case of NU-901, negligible changes in the unit cell parameters and crystallinity degree were observed (Table S5).

The thermal behaviour of thermally activated NU-1000 was studied coupling simultaneous TGA and DSC (Fig. S5a) to *in situ* TR-PXRD (Fig. S6). The latter technique was previously recurred to by Chen and coworkers[64] up to 523 K (*vs.* the 758 K of the present experiment). Along the TGA curve of the present work, the first observed mass loss of −4.6%, centred at 333 K, can be confidently attributed to the release of water molecules adsorbed from atmospheric humidity after thermal activation and sample manipulation in air, in reasonable agreement with the result of the elemental analysis (NU-1000·6.5H_2O – see Section 2.2; calculated wt% for 6.5H_2O = 5.1%). Decomposition occurs at 736 K. The residual mass at 1172 K amounts to 30.3% of the initial value and can be confidently attributed to zirconium oxide (calculated wt% for 6 ZrO_2 from NU-1000·6.5H_2O = 32.2%). As confirmed by a whole powder pattern refinement (Fig. S7a), the recovered residue consisted in a mixture of monoclinic and tetragonal ZrO_2. The DSC trace shows the absence of transformations not involving weight loss between water release and decomposition. The TR-PXRD experiment showed that NU-1000 maintains its pristine degree of crystallinity up to 678 K (Fig. S6a) and undergoes a unit cell shrinkage, overall amounting to −2.7% in the 298–678 K range, essentially due to a decrease of the crystallographic *a*-axis (hence of the hexagonal channel aperture) by −2.3% in the same temperature range (Fig. S6b and relevant caption). A contraction in the *ab*-plane was already observed by Chen *et al.* in a smaller temperature range (373–523 K).[64] Nevertheless, while they report a contraction also for the *c*-axis, we observed an increase of this axis by 2.0% in the 298–678 K range. This discrepancy may be due to the different experimental conditions adopted in the two cases: Chen *et al.* worked with a sample maintained at 423 K for 1 h prior to the TR-PXRD experiment, while we worked on a thermally activated batch manipulated under ambient conditions.

Due to its lower degree of crystallinity, the thermal stability of NU-901 was characterized only by simultaneous TGA and DSC (Fig. S5b). As for NU-1000, the first mass loss of −6.6%, centred at 337 K, could be attributed to the release of water molecules adsorbed from atmospheric humidity after sample manipulation in air, in agreement with the result of the elemental analysis (NU-901·9H_2O – see Section 2.3; calculated wt% for 9H_2O = 6.9%). Decomposition occurs at 717 K. The residual mass at 1173 K amounts to 32.2% of the initial value and can be rationalized through the formation of zirconium oxide (calculated wt% for 6 ZrO_2 from NU-901·9H_2O = 31.6%). A whole powder pattern refinement performed on the recovered residue confirmed that it consisted in a mixture of tetragonal and monoclinic ZrO_2 (Fig. S7b). As shown by the DSC curve, no transformation not involving mass loss occurs between water loss and decomposition.

3.4. Optical spectroscopy preliminary characterization in distilled water

The UV-Vis electronic absorption and fluorescence emission properties of H_4TBAPy and batches of thermally activated NU-1000 and NU-901 were studied at room temperature in distilled water suspensions with concentration of *ca.* 100 mg L^{-1}. As highlighted in the Experimental section, the suspensions were kept under magnetic stirring until they were used; moreover, after

the addition of an aliquot of water or analyte, the cuvette was gently shaken till the suspension appeared homogeneous at the naked eye. The UV-Vis electronic absorption properties of the selected POPs (Scheme 1) were investigated at room temperature in 50 μM aqueous solutions. When excited at $\lambda_{ex} = 433$ nm (corresponding to its maximum absorption wavelength), H_4TBAPy shows a broad fluorescence emission band peaking at $\lambda_{fluo,max} = 538$ nm (Fig. 4a), in the yellow-green region of the visible electromagnetic spectrum. This evidence agrees with the emission maximum observed for H_4TBAPy in the solid state (529 nm),[65] while it differs from the results obtained for $TBAPy^{4-}$ in a basic aqueous solution (440 nm).[65] In the case of NU-1000, $\lambda_{abs,max}$ and $\lambda_{fluo,max}$ are blue-shifted with respect to the ligand (exemplary values = 411 nm and 463 nm, respectively; Fig. 4b). Worthy of note, and in agreement with what previously reported in the literature (Table S6), in the adopted experimental conditions NU-1000 $\lambda_{fluo,max}$ was found to be batch-dependent, with actual emission maxima laying in the range 463–501 nm, in the blue-green region of the electromagnetic spectrum. This variability, never explicitly addressed before, could be attributed to specific crystallochemical features such as presence and amount of clathrated solvent, trace residual modulator at the nodes, missing linker defects. Finally, the absorption and emission spectra of NU-901 largely reproduce those of the parent ligand (Fig. 4c), with $\lambda_{abs,max}$ and $\lambda_{fluo,max}$ laying at 435 nm and 535 nm, respectively, thus showing a smaller shift with respect to that observed for NU-1000. For comparison, the observed emission maximum is in fair agreement with the value of 518 nm recorded by Ning *et al.* in similar experimental conditions.[43] Beyond the potential role of the crystallochemical variables quoted above, the different photophysical behaviour of the two MOFs can be reasonably attributed to their structural features (see Section 3.2): as demonstrated combining experimental results and theoretical calculations,[66] the different relative orientation and distance of the ligands in NU-1000 and NU-901 could give rise to specific interchromophoric interactions, resulting in different electronic transition energies for each of the two materials and the free linker. Finally, the UV-Vis electronic absorption properties of the selected POPs in aqueous solutions were independently confirmed. As shown in Fig. S8, collectively proposing the five absorption spectra, no POP absorbs in the spectral range we subsequently used for the luminescence sensing tests (411–700 nm and 445–700 nm for NU-1000 and NU-901, respectively). For completeness, Table S7 collects the $\lambda_{abs,max}$ observed in this study for the five POPs at comparison with what reported in the literature in similar experimental conditions.[67]

3.5. NU-1000 and NU-901 luminescence emission as a function of dilution in distilled water

The operative protocol used for the first round of sensing experiments (Protocol 1; see Section 2.7) implied subsequent additions of POP aqueous solution aliquots to a 2 mL MOF

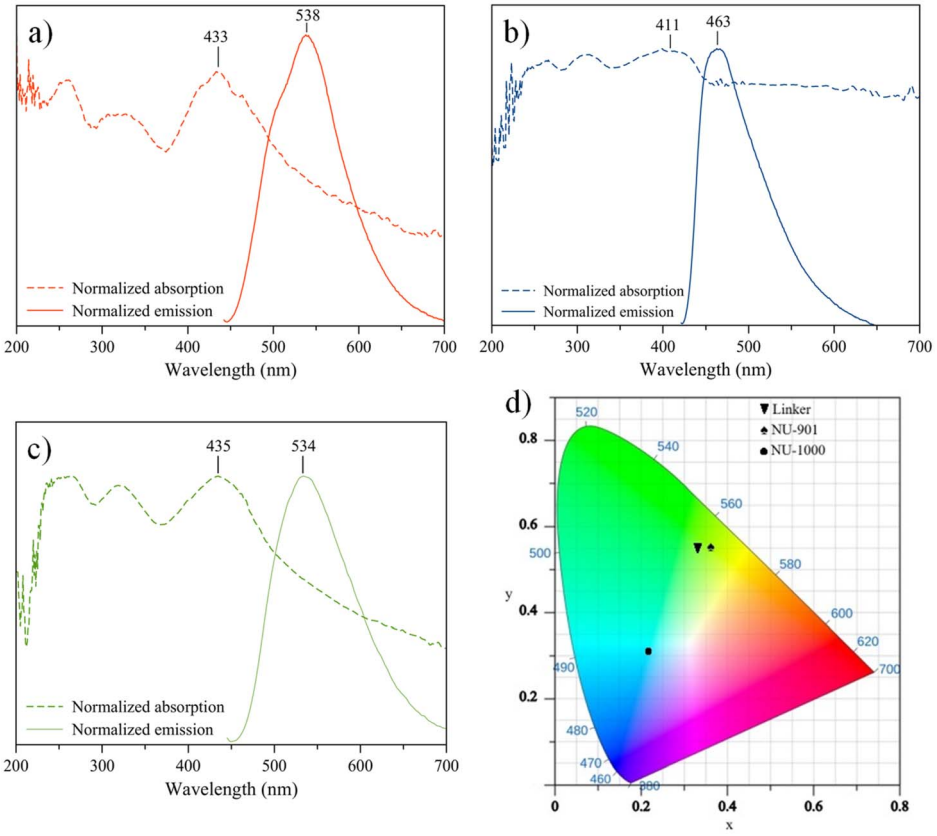

Fig. 4 Normalized absorption (dashed lines) and emission (solid lines) spectra of (a) H_4TBAPy, (b) NU-1000 and (c) NU-901, measured at room temperature in *ca.* 100 mg L^{-1} distilled water suspensions. (d) CIE-1931 diagram (calculated using the free online tool described in 68).

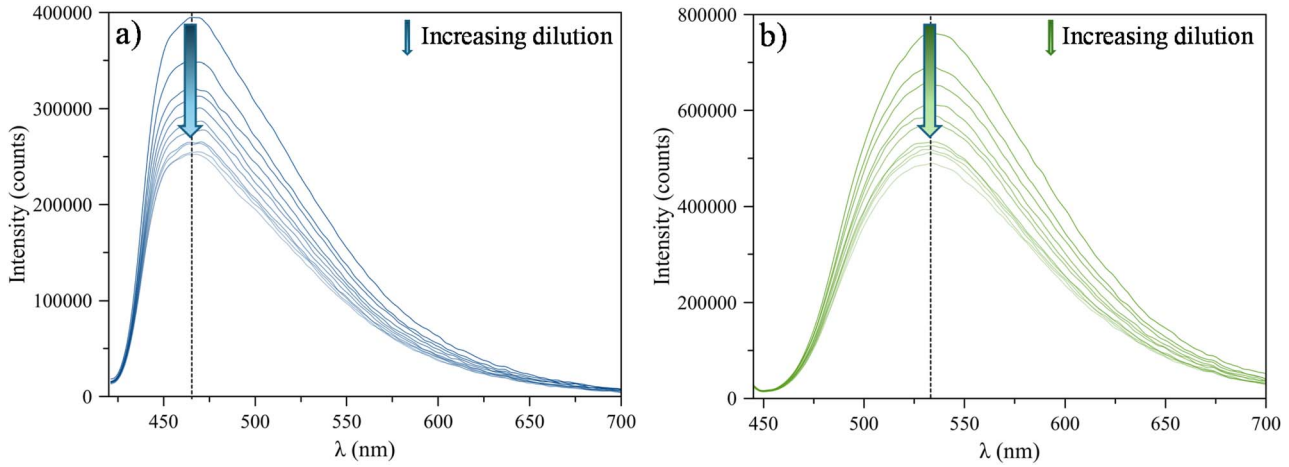

Fig. 5 Fluorescence emission spectra of distilled water suspension of (a) NU-1000 and (b) NU-901 as a function of dilution.

suspension, up to a total added volume of *ca.* 0.5 mL. Based on this protocol, we firstly investigated the influence of MOF dilution on its emission spectrum. As expected, both MOFs undergo a monotonic emission intensity decrease as their suspension is progressively diluted, while no change affects the emission maximum or spectrum shape (Fig. 5). As shown in Fig. 6, for both MOFs the absolute intensity variation (ΔI; eqn (1)) as a function of dilution could be fitted with an exponential function, whose equation was subsequently employed to discriminate the intensity variation due to the presence of POPs from that due to dilution. The fitting was performed in the same volume range later used for the sensing tests, so that no extrapolation of the MOFs behaviour upon dilution was necessary. As discussed below, assessment of the role of dilution was crucial for NU-1000, as we observed that the adopted POPs caused an intensity quenching. Worthy of note, despite the key role that sensor dilution could play, as shown by this study case, in previous studies adopting a protocol similar to ours the influence of this parameter on the sensor performance was often overlooked.

3.6. NU-1000 sensing performance in distilled water

As shown in Fig. 7a for DCF and Fig. S9 for PAR, ACA and FXT, in distilled water and adopting Protocol 1 the selected contaminants caused a decrease of NU-1000 emission intensity, while no variation of $\lambda_{fluo,max}$ or overall spectrum shape was observed. Worthy of note, as assessed by three replicates performed starting with fresh MOF suspensions (prepared with the same MOF sample) and POP solutions, in all the cases the observed behaviour was reproducible. In addition, a comparison of the emission intensity quenching observed during POPs addition with that due to dilution (see Section 3.5) disclosed that the ΔI observed in presence of PAR, ACA and FXT is not distinguishable from that due to dilution of the MOF (see Fig. S9). This occurrence suggests that no modification in the emission properties of the MOF is triggered by those pollutants in the adopted experimental conditions. On the other hand, as shown in Fig. 7b the emission intensity quenching due to DCF is different from that due to dilution, hence is genuinely due to the presence of the pollutant. To confirm the selectivity of the MOF toward DCF, the emission intensity variation due to all the POPs at a representative concentration amounting to 6.3 μM

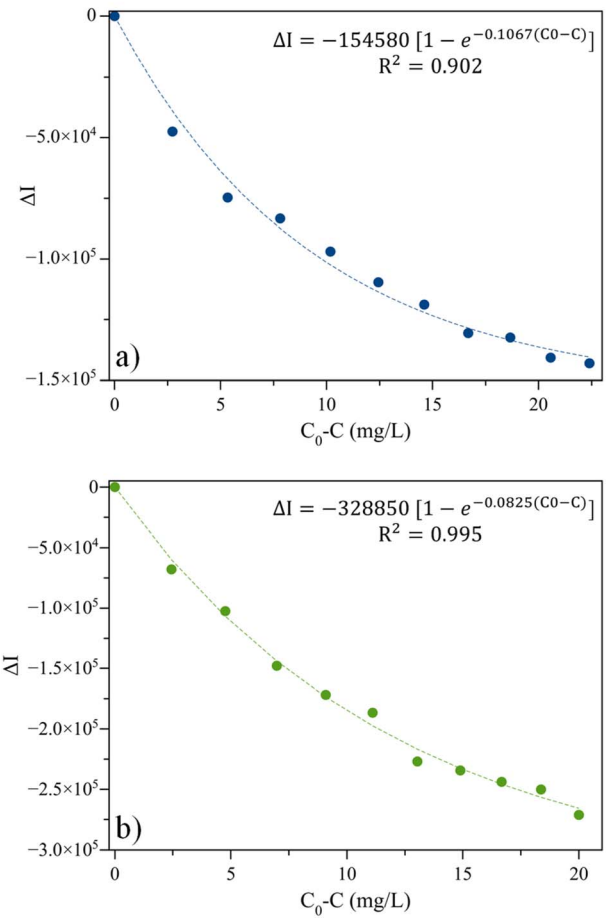

Fig. 6 Intensity variation (ΔI) as a function of MOF concentration (expressed as C_0-C, where C_0 is the initial concentration while C is the actual concentration) for (a) NU-1000 and (b) NU-901. The fitting curves, whose equations are reported as insets, are depicted as dashed lines.

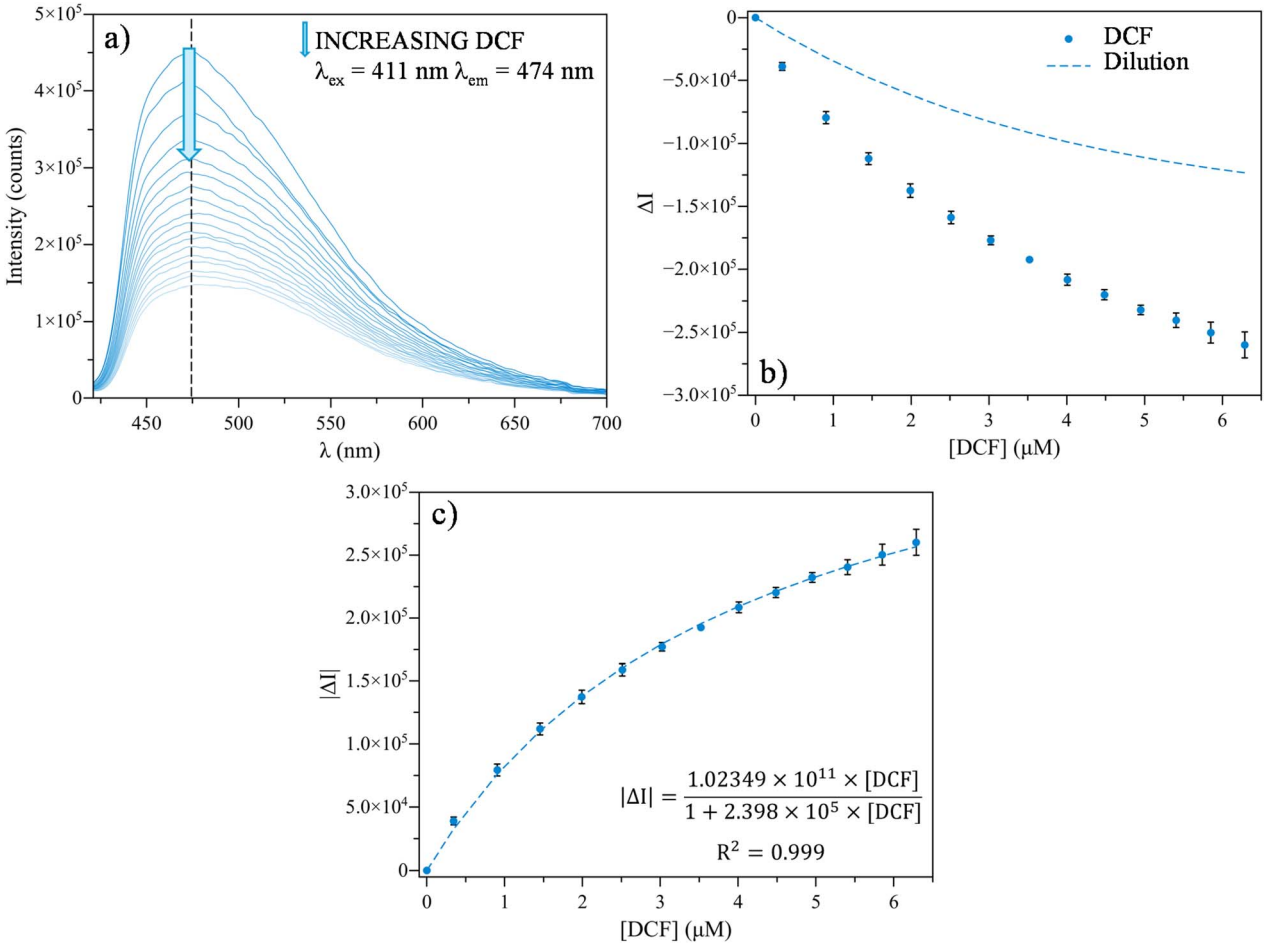

Fig. 7 (a) Fluorescence emission spectra of a distilled water suspension of NU-1000 at increasing concentration of DCF. (b) Emission intensity variation (ΔI) averaged over three replicates as a function of DCF concentration. According to what reported in Section 3.5, the variation of the emission intensity due to dilution is depicted as a dashed line. (c) Fitting of the average emission intensity variation with a binding function. In (b) and (c) the vertical bars represent the standard deviation of the three replicates.

was compared as explained in Section 2.7. An analysis of variance (Single Factor ANOVA) yielded a *P*-value of 1.1×10^{-7} ($\alpha = 0.05$), indicating that the response of NU-1000 toward at least one POP is statistically different from that triggered by the others. Tukey's Honest Significant Difference test[57] (Table S8) identified DCF as the contaminant statistically different from the others [q_{cal}(DCF *vs.* PAR, ACA, FXT) > q_{crit}]. On the contrary, PAR, ACA and FXT are not distinguishable from each other ($q_{cal} < q_{crit}$ for any of the couples). These statistically validated results suggest that NU-1000 can be successfully employed as selective sensor for DCF over the remaining investigated pollutants in the adopted experimental conditions.

Prompted by these promising results, we decided to gain a deeper insight on the NU-1000/DCF couple. Modelling the average emission intensity variation in the 0–6.3 μM range with a binding function[58] (eqn (2) and Fig. 7c), we retrieved a binding constant, K_a, amounting to $2.4(1) \times 10^5$ M^{-1} and we concomitantly demonstrated that, beyond detection, DCF quantification is feasible in the essayed experimental conditions. Finally, applying eqn (3) and (4) on the 0–1.45 μM concentration range, we retrieved a limit of detection of 5×10^{-1} μM (1.6×10^{-4} g L^{-1}) (Fig. S10). This value is definitely higher than the mean concentration reported for DCF in European surface water bodies (27–47 ng L^{-1})[69] and groundwaters (1.4–5300 ng L^{-1}),[46] and the predicted no-effect concentration (PNEC) for DCF in surface water (50 ng L^{-1}).[69] Yet, as anticipated in the Introduction, the main aim of the present investigation is emphasizing the relevance, when applying MOFs as luminescent sensors in water, of assessing the reproducibility of sensor performance and the role of sensor dilution. Accordingly, a comparison of the LoD estimated in the present work with that reported for DCF sensing by other MOFs applying an experimental approach similar to Protocol 1 but disregarding the above quoted aspects appears somehow not fully pertinent. Nevertheless, for the sake of comparison, we report in Table S9 the LoD values retrieved in past works using a similar protocol and different Zr^{IV} or Zn^{II} MOFs.

3.7. NU-901 sensing performance in distilled water

When tested as sensor for DCF, PAR, ACA and FXT in distilled water solutions of concentration 0.3–9.5 μM, NU-901 showed reproducible results only in presence of DCF and PAR (Fig. 8

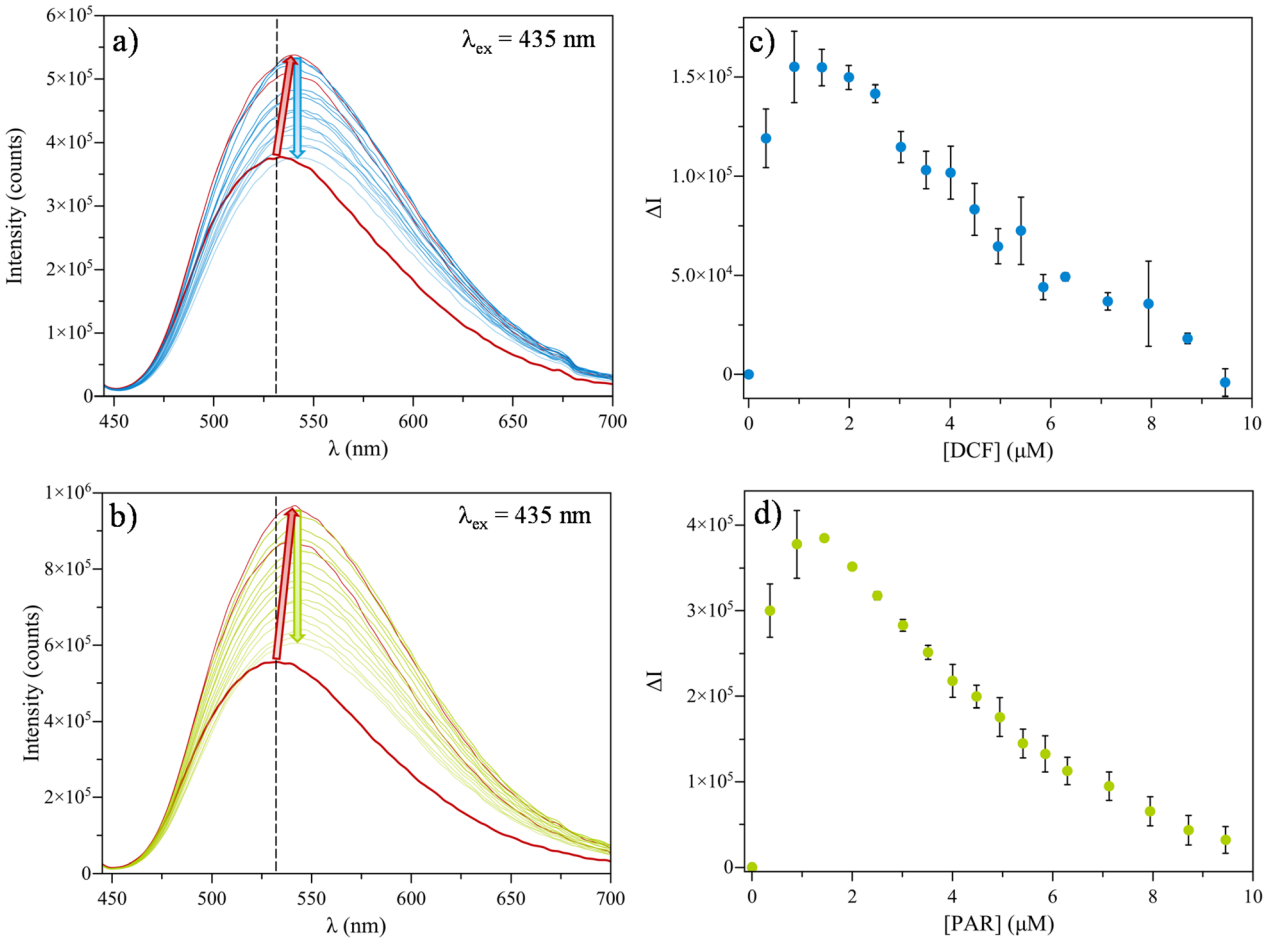

Fig. 8 Fluorescence emission spectra of a distilled water suspension of NU-901 at increasing concentration of (a) DCF and (b) PAR. The spectra corresponding to an increase in the emission intensity are depicted in red, while those corresponding to luminescence quenching are depicted in blue and green for DCF and PAR, respectively. Emission intensity variation (Δ*I*), averaged over three replicates, as a function of the concentration of (c) DCF and (d) PAR. In (c and d) the vertical bars represent the standard deviation of the three replicates.

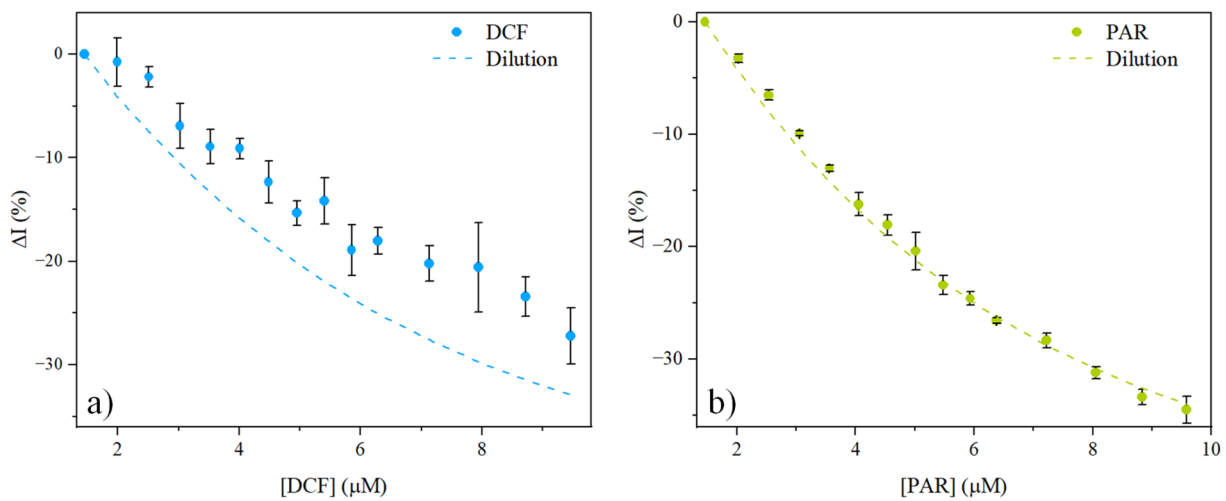

Fig. 9 Comparison between the Δ*I*(%) observed along the decreasing branches of Fig. 8 as a function of (a) [DCF] and (b) [PAR] and the Δ*I*(%) due to NU-901 dilution in the same concentration range.

and S11). In both cases, the emission intensity varies following a non-monotonic trend, namely: an initial intensity increase, up to a concentration of *ca.* 1.45 μM for both POPs, is followed by a luminescence quenching. Moreover, a slight bathochromic shift (*ca.* 10 nm) of $\lambda_{fluo,max}$ was observed along with the increase of the emission intensity (Fig. 8). At variance, no shift of the maximum wavelength was observed in presence of FXT and ACA (Fig. S11) or during the dilution experiment (Fig. 5b).

The increase in emission intensity could be ascribed to the occurrence of interactions between the POPs and the MOF surface up to a maximum where the MOF reaches saturation and no more POP can interact with it. As anticipated in the Introduction, an emission intensity enhancement is one of the phenomena that could occur when fluorescent materials are applied as sensors, as already observed, for example, for other Zr-based MOFs.[70,71] The subsequent luminescence quenching might be due to the dilution of the sensor. To demonstrate this hypothesis, along the decreasing branch the emission intensity relative variation [$\Delta I(\%)$] due to PAR and DCF was calculated starting from the highest point of the curve in Fig. 8c and d, respectively, according to eqn (5):

$$\Delta I(\%) = \frac{I_x - I_0}{I_0} \times 100 \quad (5)$$

where I_x and I_0 are the maximum intensity at a given POP concentration and at the zero-point, respectively. $\Delta I(\%)$ was then compared with the function describing the behaviour of $\Delta I(\%)$ *vs.* [NU-901] upon dilution. The outcomes of the comparison, shown in Fig. 9, nicely confirm that the decreasing branch in Fig. 8c and d is caused by dilution.

To verify the potential selectivity of NU-901 toward DCF over PAR (or *vice versa*), a Student's *t*-test was carried out considering the ΔI caused by the two POPs at the exemplary concentration of 1.45 μM. The test was carried out considering a two-tailed distribution and assuming the same variance for the two samples [based on a previous *F*-test, $F_{tab}(2,2) = 19$, $F_{stat} = 0.05$]. The test results showed that there is a statistically significant difference between the ΔI caused by the two substances [t_{tab} (df = 4) = 2.78, $t_{stat} = 42.4$].

To further assess the sensing properties of NU-901 at low DCF and PAR concentration concomitantly ruling out the contribution of dilution, we modified the analysis protocol (adopting Protocol 2; see Section 2.7).

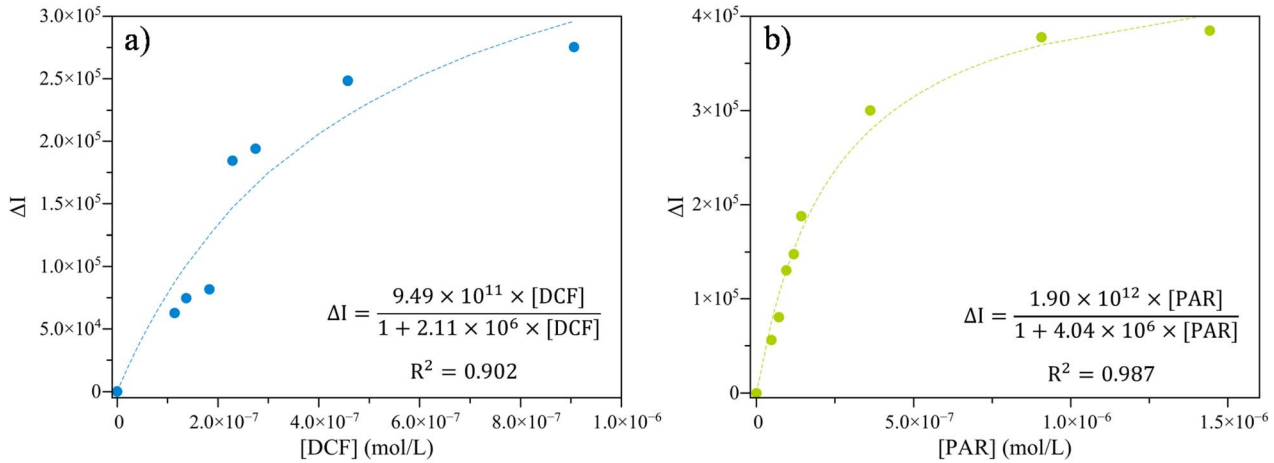

Fig. 10 NU-901 emission intensity variation as a function of the concentration of (a) DCF and (b) PAR up to a value of 1.5 μM. The binding function modelling the datapoints is depicted as a dashed line. The relevant equation is reported as inset.

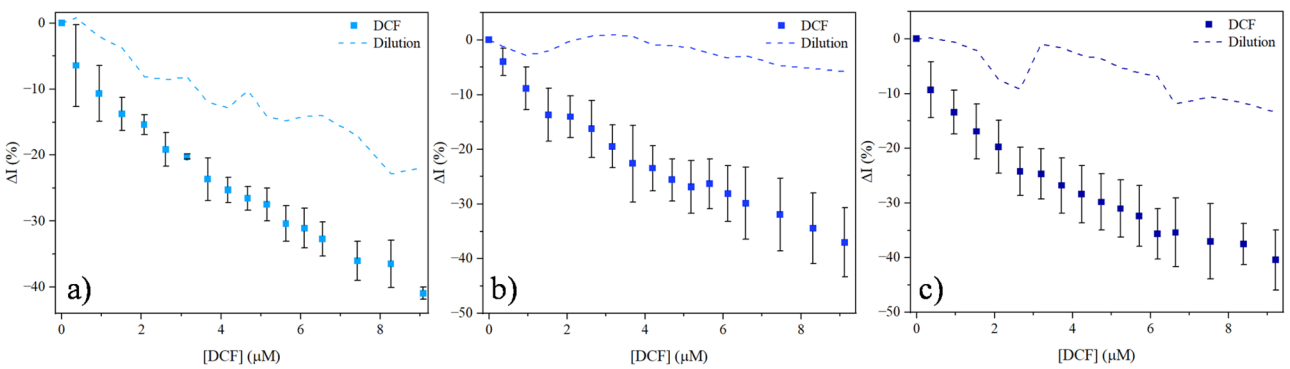

Fig. 11 NU-1000 emission intensity relative variation at increasing DCF concentration in (a) distilled water, (b) bottled water and (c) tap water. The vertical bars represent the standard deviation of the three replicates.

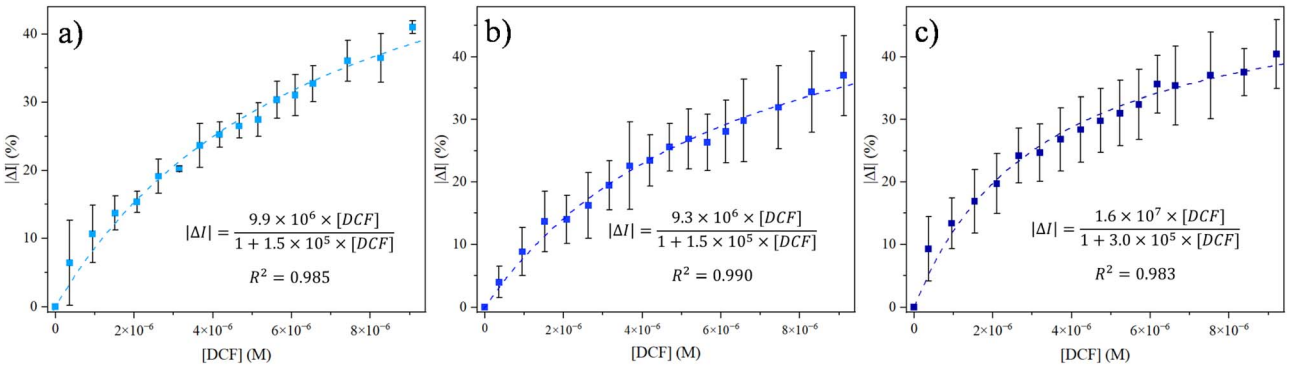

Fig. 12 NU-1000 emission intensity relative variation in (a) distilled water, (b) bottled water, and (c) tap water modelled using a binding function. The vertical bars represent the standard deviation of the three replicates.

The obtained values of ΔI could be mathematically modelled using a binding function (Fig. 10), retrieving binding constants of $4.0(6) \times 10^6$ M^{-1} and $2(1) \times 10^6$ M^{-1}, for paracetamol and diclofenac sodium, respectively, one order of magnitude higher than those obtained for the couple NU-1000/DCF. This occurrence could be related to the insurgence of stronger interactions between NU-901 and DCF or PAR. Parallel to this, working on the 0–2.7×10^{-1} and 0–1.4×10^{-1} μM concentration range for DCF and PAR, respectively, limits of detection of *ca.* 3×10^{-1} and 4×10^{-2} μM (9.5×10^{-5} and 6.1×10^{-6} g L^{-1}) were obtained (see Fig. S12 for the relevant linear regression plots).

3.8. NU-1000 sensing performance in different water matrices

Based on the promising results of the sensing experiments carried out in distilled water, we selected the couple NU-1000/DCF to study the influence of the pollutant water matrix on the MOF sensing performances. These experiments were carried out adopting Protocol 3 (see Section 2.8) and a fresh batch of NU-1000, different from that used for the above reported experiments. Remarkably, as shown by Fig. 11, the response of NU-1000 in the three water matrices is comparable: in all cases there is a decrease of the emission intensity at increasing DCF concentration, while no change in the emission maximum or overall spectra shape is observed. All the curves could be successfully modelled using a binding function, as shown by Fig. 12: notably, comparable binding constants were retrieved for the three water matrices (Table 1). Noteworthy, these values are in nice accordance even with that recovered upon treating the data obtained along Protocol 1 (Table 1), this occurrence demonstrating the robustness of the proposed approach.

A linear fitting of the first part of the curves shown in Fig. 12, followed by application of eqn (3) and (4) enabled also the estimation of DCF limits of detection, which are analogous in the different matrices and across different protocols (Table 1), confirming that the performances of NU-1000 as DCF sensor are not affected by the chemical composition of the water matrix. Additionally, as these experiments were performed with a new batch of NU-1000, we also proved that its sensing ability (as *per* estimated LoD and binding constant) is not affected by the batch-to-batch variability of the emission highlighted in Section 3.4.

Table 1 Binding constants and limits of detection retrieved adopting Protocols 1 and 3 for the couple NU-1000/DCF in different water matrices

Water matrix	Protocol	K_a (M^{-1})	LoD (μM)
Distilled water	1	$2.4(1) \times 10^5$	5×10^{-1}
Distilled water	3	$1.5(2) \times 10^5$	8×10^{-1}
Bottled water	3	$1.5(2) \times 10^5$	7×10^{-1}
Tap water	3	$3.0(4) \times 10^5$	9×10^{-1}

4. Conclusions

This case study evaluated the two MOFs NU-1000 and NU-901 as luminescent sensors of four waterborne persistent organic pollutants (POPs) to pinpoint the relevance, in this applicative context, of a standardized and statistically grounded protocol ensuring results reproducibility and reliability. The outcomes presented above demonstrated that, in distilled water, NU-1000 exhibited a reproducible response across all the investigated contaminants in the concentration range 0.3–9.5 μM. Nonetheless, its response was distinguishable from that due to its simple dilution only with diclofenac sodium. Toward the latter NU-1000 showed a reproducible and comparable performance even in bottled and tap water and under two different experimental protocols, with an affinity (estimated through the binding constant) and limit of detection on the order of 10^5 M^{-1} and 10^{-1} μM, respectively. At variance, in similar experimental conditions NU-901 showed a reproducible behaviour only with diclofenac sodium and paracetamol, with a non-monotonic trend due to the prevalent contribution of MOF/POP interactions at low POP concentration and of sensor dilution at concentrations higher than 1.5 μM. Overall, this case study successfully strengthened the importance, in the addressed applicative domain, of taking into due consideration crucial features as statistically validated reproducibility of the sensor performance, operative conditions such as sensor dilution, transferability of the performance in different working

matrices. As such, this work contributes to pave the way toward improved porous material-based sensing systems.

Author contributions

AM: investigation, formal analysis, validation, writing – original draft, review & editing. GC: Investigation, formal analysis, writing – review & editing. SG: conceptualization, supervision, validation, funding acquisition, writing – original draft, review & editing.

Conflicts of interest

There are no conflicts of interest to declare.

Data availability

Data for this article, including infrared, ^{1}H-NMR and X-ray fluorescence spectra, powder X-ray diffraction patterns, thermograms, UV-Vis electronic adsorption and fluorescence emission spectra, are available in the form of ascii files at the authors upon request.

Supplementary information (SI): ^{1}H NMR spectra of NU-1000 and NU-901; IR spectra of H_4TBAPy, NU-1000 and NU-901; XRF spectra of NU-1000 and NU-901; PXRD patterns of NU-1000 and NU-901 and relevant whole powder pattern refinements; simultaneous TGA and DSC traces of NU-1000 and NU-901; TR-PXRD patterns of NU-1000 and relevant unit cell parameters behaviour; PXRD qualitative analysis of the residue recovered at the end of the thermal analysis of NU-1000 and NU-901; UV-Vis electronic absorption spectra of distilled water solutions of DCF, FXT, PAR and ACA; fluorescence emission spectra of NU-1000 at increasing concentration of ACA, FXT and PAR, and relevant data treatment; linear regression to estimate the LoD for the couples NU-1000/DCF, NU-901/DCF and NU-901/PAR; NU-901 relative intensity variation at increasing amount of FXT and ACA; volumes of POPs mother solutions added to the cuvette; reported chemico-physical analysis of the samples of bottled and tap water used in this study; results of whole powder pattern refinements performed on the PXRD patterns of samples of NU-1000 and NU-901 acquired before and after suspension in water; NU-1000 emission maxima found in the literature; POPs experimental absorption maxima found in the literature; Tukey's HSD test results. See DOI: https://doi.org/10.1039/d6ta00023a.

Acknowledgements

This work was carried out within the project 2022A3XNWJ, "Wastewater treatment and monitoring with luminescent mixed-linker Metal–Organic Frameworks as chemical sensors and adsorbents of Contaminants of Emerging Concern (LUMIMOF)", funded by the Ministero dell'Università e della Ricerca within the PRIN 2022 program (D.D.104 02/02/2022), funded by the European Union – Next Generation EU. AM acknowledges Università degli Studi dell'Insubria for a three-year Ph.D. scholarship. Scientific support from the CRIETT centre of the Università degli Studi dell'Insubria (instruments codes: MAC01, MAC04, MAC08, and MAC12) is acknowledged.

Notes and references

1 O. M. L. Alharbi, A. Arsh Basheer, R. A. Khattab and I. Ali, *J. Mol. Liq.*, 2018, **263**, 442.
2 D. C. G. Muir and P. H. Howard, *Environ. Sci. Technol.*, 2006, **40**, 7157.
3 F. B. Awino and G. Garland, *Environ. Chall.*, 2025, **18**, 101094.
4 Y.-F. Li, S. Hao, W.-L. Ma, P.-F. Yang, W.-L. Li, Z.-F. Zhang, L.-Y. Liu and R. W. Macdonald, *Environ. Sci. Ecotechnol.*, 2024, **18**, 100311.
5 W. Guo, X. Ji, Z. Yu, H. Jiang and X. Guan, *J. Earth Sci.*, 2024, **35**, 729.
6 J. Walkowiak, J.-A. Wiener, A. Fastabend, B. Heinzow, U. Krämer, E. Schmidt, H.-J. Steingrüber, S. Wundram and G. Winneke, *Lancet*, 2001, **358**, 1602.
7 G. Ross, *Ecotoxicol. Environ. Saf.*, 2004, **59**, 275.
8 G. Venkatraman, N. Giribabu, P. S. Mohan, B. Muttiah, V. K. Govindarajan, M. Alagiri, P. S. A. Rahman and S. A. Karsani, *Chemosphere*, 2024, **351**, 141227.
9 N. Mathew, A. Somanathan, A. Tirpude, A. M. Pillai, P. Mondal and T. Arfin, *Anal. Methods*, 2025, **17**, 1698.
10 M. Zaynab, M. Fatima, Y. Sharif, K. Sughra, M. Sajid, K. A. Khan, A. H. Sneharani and S. Li, *Science*, 2021, **33**, 101511.
11 Z. Singh, J. Kaur, R. Kaur and S. Singh Hundal, *Am. J. BioSci.*, 2016, **4**, 11.
12 Y. Zhang, S.-U. Geißen and C. Gal, *Chemosphere*, 2008, **73**, 1151.
13 United Nations, *Goal 6: Ensure Availability and Sustainable Management of Water and Sanitation for All, SDG Knowledge Platform*, https://sdgs.un.org/goals/goal6, website last access: February 2026.
14 See *e.g.* (*a*) *Joint Monitoring Programme for Water Supply and Sanitation*, https://washdata.org/, website last access: February 2026; (*b*) *Global Coalition for Better Policies and Regulation of Water and Sanitation Services*, https://liswater.org/en/global-coalition-for-better-policies-and-regulation/, website last access: February 2026.
15 See *e.g.*, the Stockholm Convention: (*a*) W. Xu, X. Wang and Z. Cai, *Anal. Chim. Acta*, 2013, **790**, 1; (*b*) P. E. Hagen and M. P. Walls, *Nat. Resour. Environ.*, 2005, **19**, 49.
16 O. M. Yaghi, M. Kalmutzki and C. S. Diercks, *Introduction to Reticular Chemistry*, Wiley-VCH, 2019.
17 F. Caroleo, G. Magna, M. L. Naitana, L. Di Zazzo, R. Martini, F. Pizzoli, M. Muduganti, L. Lvova, M. Mandoj, S. Nardis, M. Stefanelli, C. Di Natale and R. Paolesse, *Sensors*, 2022, **22**, 2649.
18 M. Wagner, K.-Y. A. Lin, W.-D. Oh and G. Lisak, *J. Hazard. Mater.*, 2021, **413**, 125325.
19 S. Rojas and P. Horcajada, *Chem. Rev.*, 2020, **120**, 8378.
20 W. Cheng, X. Tang, Y. Zhang, D. Wu and W. Yang, *Trends Food Sci. Technol.*, 2021, **112**, 268.
21 H. Sohrabi, S. Ghasemzadeh, Z. Ghoreishi, M. R. Majidi, Y. Yoon, N. Dizge and A. Khataee, *Mater. Chem. Phys.*, 2023, **299**, 127512.

22 X. Lu, K. Jayakumar, Y. Wen, A. Hojjati-Najafabadi, X. Duan and J. Xu, *Microchim. Acta*, 2024, **191**, 58.
23 G.-L. Yang, X.-L. Jiang, H. Xu and B. Zhao, *Small*, 2021, **17**, 2005327.
24 T. K. Pal, *Mater. Chem. Front.*, 2023, **7**, 405.
25 S. Jensen, K. Tan, W. Lustig, D. Kilin, J. Li, Y. J. Chabal and T. Thonhauser, *J. Mater. Chem. C*, 2019, **7**, 2625.
26 P. Rani, A. Husain, K. K. Bhasin and G. Kumar, *Inorg. Chem.*, 2024, **63**, 3486.
27 N. Lei, W. Li, D. Zhao, W. Li, X. Liu, L. Liu, J. Yin, M. Muddassir, R. Wen and L. Fan, *Spectrochim. Acta A*, 2024, **306**, 123585.
28 W.-M. Chen, J.-J. Shao, Y. Zhang, Z.-D. Xue, P.-L. Liu, J.-L. Ni, L.-Z. Chen, Q. Gao and F.-M. Wang, *J. Mol. Struct.*, 2024, **1297**, 137007.
29 X. Yu, D. I. Pavlov, A. A. Ryadun, K. A. Kovalenko, T. Y. Guselnikova, E. Benassi, A. S. Potapov and V. P. Fedin, *Angew. Chem., Int. Ed.*, 2024, **63**, e202410509.
30 Y. Jiang, X. Fang, Y. Ni, J. Huo, Q. Wang, Y. Liu, X. Wang and B. Ding, *Chem. Eng. J.*, 2024, **479**, 147232.
31 J. Li, S. Zhang, L. Fan, Y. Yang and R. Wen, *Appl. Organomet. Chem.*, 2024, **39**, e7887.
32 H. Zhao, H. Li, J. Zhang, H. Yan, J. Lu, H. Liu, H. Hao, J. Dou, Y. Li and S. Wang, *Inorg. Chem.*, 2024, **63**, 1962.
33 L. Chen, Z. Li, Y. Dou, H. Wang, C. Chen and X. Wang, *J. Hazard. Mater.*, 2024, **469**, 134045.
34 X. Fang, Z. Jiang, X. Zhou, J. Du, Y. Jiang, D. Wang, X. Wang and B. Ding, *ACS Appl. Nano Mater.*, 2024, **7**, 1940.
35 J. Zhao, P. Li, Q. Zhang, Z. Ye, Y. Wang, J. Tian, Z. Xu, N. Peng, H. Ren and X. Zhang, *Chem. Eng. J.*, 2024, **499**, 156184.
36 L. F. Yang, Z. Fu, J. Xie and Z. Ding, *Food Res. Int.*, 2024, **197**, 115272.
37 J. E. Mondloch, W. Bury, D. Fairen-Jimenez, S. Kwon, E. J. DeMarco, M. H. Weston, A. A. Sarjeant, S. T. Nguyen, P. C. Stair, R. Q. Snurr, O. K. Farha and J. T. Hupp, *J. Am. Chem. Soc.*, 2013, **135**, 10294.
38 S. J. Garibay, I. Iordanov, T. Islamoglu, J. B. DeCoste and O. K. Farha, *CrystEngComm*, 2018, **20**, 7066.
39 (*a*) S. Yuan, J.-S. Qin, C. T. Lollar and H.-C. Zhou, *ACS Cent. Sci.*, 2018, **4**, 440; (*b*) R. J. Drout, L. Robinson, Z. Chen, T. Islamoglu and O. K. Farha, *Trends Chem.*, 2019, **1**, 304.
40 T. C. Wang, N. A. Vermeulen, I. S. Kim, A. B. F. Martinson, J. F. Stoddart, J. T. Hupp and O. K. Farha, *Nat. Protoc.*, 2016, **11**, 149.
41 L. Luconi, G. Mercuri, T. Islamoglu, A. Fermi, G. Bergamini, G. Giambastiani and A. Rossin, *J. Mater. Chem. C*, 2020, **8**, 7492.
42 W. Hao, G. Huang, G. Jiang, S. A. Dauda and F. Pi, *Food Biosci.*, 2023, **55**, 102967.
43 D. Ning, Q. Liu, Q. Wang, X. Du, Y. Li and W. Ruan, *Dalton Trans.*, 2019, **48**, 5705.
44 S. Sun, C. Wei, Y. Xiao, G. Li and J. Zhang, *RSC Adv.*, 2020, **10**, 44912.
45 The Medicines Utilisation Monitoring Centre, *National Report on Medicines Use in Italy*, Italian Medicines Agency, Rome, 2025.
46 C. Duarte, T. Di Lorenzo and A. S. P. S. Reboleira, *Sci. Rep.*, 2024, **14**, 20689.
47 L. Albarano, C. Maggio, G. Lofrano, M. Carotenuto, M. Guida, V. Vaiano and G. Libralato, *J. Hazard. Mater.*, 2025, **499**, 140107.
48 M. Pagano, S. Savoca, F. Impellitteri, M. Albano, G. Capillo and C. Faggio, *Front. Physiol.*, 2022, **13**, 920952.
49 *Selection of Substances for the 5th Watch List under the Water Framework Directive*, Publications Office of the European Union, 2025, DOI: 10.2760/956398.
50 J. M. Martin, M. G. Bertram, M. Saaristo, T. E. Ecker, S. L. Hannington, J. L. Tanner, M. Michelangeli, M. K. O'Bryan and B. B. M. Wong, *Sci. Total Environ.*, 2019, **650**, 1771.
51 A. Le Bail, *Powder Diffr.*, 2005, **20**, 316.
52 *TOPAS-R v. 3.0*, Bruker AXS GmbH, Karlsruhe, Germany, 2005.
53 L. Robison, R. J. Drout, L. R. Redfern, F. A. Son, M. C. Wasson, S. Goswami, Z. Chen, A. Olszewski, K. B. Idrees, T. Islamoglu and O. K. Farha, *Chem. Mater.*, 2020, **32**, 3545.
54 N. Planas, J. E. Mondloch, S. Tussupbayev, J. Borycz, L. Gagliardi, J. T. Hupp, O. K. Farha and C. J. Cramer, *J. Phys. Chem. Lett.*, 2014, **5**, 3716.
55 A. Pankajakshan, M. Sinha, A. A. Ojha and S. Mandal, *ACS Omega*, 2018, **3**, 7832.
56 *MATLAB Version 23.2.0 (R2023b), Update 4*.
57 D. C. Howell, *Statistical Methods for Psychology*, Wadsworth Cengage Learning, 7th edn, 2010, ch. 12.
58 J. Li, Y. Chen, T. Chen, J. Qiang, Z. Zhang, T. Wei, W. Zhang, F. Wang and X. Chen, *Sens. Actuators, B*, 2018, **268**, 446.
59 Each node is composed of six Zr^{IV} ions, which lay at the vertices of an octahedron and are eight-coordinated in a square antiprismatic geometry; one face of the antiprism is defined by two OH^- and two O^{2-} ligands, while the other face of the is defined by either four oxygen atoms belonging to the carboxylate groups of the linker in the case of one independent Zr^{IV} ion, or two oxygen atoms belonging to the linker carboxylate groups plus one H_2O and one OH^- ligands for the other independent Zr^{IV} ion. The faces of the octahedral cluster are tricapped by OH^-/O^{2-} ligands.
60 In NU-1000, the triangular channel diameter was estimated as the diameter of the sphere inscribed in a prism with triangular base whose edge is the shortest Zr···Zr distance. The hexagonal channel diameter was estimated considering the distance between two oxygen atoms at the opposite vertices of the hexagon and subtracting twice the van der Waals radius of oxygen (152 pm), A. Bondi, *J. Phys. Chem.*, 1964, **68**, 441.
61 In NU-1000, the window aperture was estimated considering the shortest O···O distance between facing oxygen atoms and subtracting twice the van der Waals radius of oxygen (152 pm).
62 In NU-901, the channel diameter and window aperture were estimated considering the shortest O···O distance between

facing oxygen atoms and subtracting twice the van der Waals radius of oxygen (152 pm).

63 (*a*) P. Deria, Y. G. Chung, R. Q. Snurr, J. T. Hupp and O. K. Farha, *Chem. Sci.*, 2015, **6**, 5172; (*b*) L. Yang, K. B. Idrees, Z. Chen, J. Knapp, Y. Chen, X. Wang, R. Cao, X. Zhang, H. Xing, T. Islamoglu and O. K. Farha, *ACS Appl. Nano Mater.*, 2021, **4**, 4346.

64 Z. Chen, G. D. Stroscio, J. Liu, Z. Lu, J. T. Hupp, L. Gagliardi and K. W. Chapman, *J. Am. Chem. Soc.*, 2023, **145**, 268.

65 K. C. Stylianou, R. Heck, S. Y. Chong, J. Bacsa, J. T. A. Jones, Y. Z. Khimyak, D. Bradshaw and M. J. Rosseinsky, *J. Am. Chem. Soc.*, 2010, **132**, 4119.

66 P. Deria, J. Yu, T. Smith and R. P. Balaraman, *J. Am. Chem. Soc.*, 2017, **139**, 5973.

67 (*a*) DCF: D. R. Lima, A. A. Gomes, E. C. Lima, C. S. Umpierres, P. S. Thue, J. C. P. Panzenhagen, G. L. Dotto, G. A. El-Changhaby and W. S. de Alencar, *Spectrochim. Acta A*, 2019, **218**, 366; (*b*) PAR: T. Bouarroudj, L. Aoudjit, I. Nessaibia, D. Zioui, Y. Messai, A. Bendjama, S. Mezrag, M. Chabbi and K. Bachari, *Russ. J. Phys. Chem.*, 2023, **97**, 1074; (*c*) FXT: M. W. Lam, C. J. Young and S. A. Mabury, *Environ. Sci. Technol.*, 2005, **39**, 513; (*d*) ACA: M. Nayak, C. B. Patel, A. Mishra, R. Singh and R. K. Singh, *J. Fluoresc.*, 2024, **34**, 1441.

68 E. H. H. Hasabeldaim, H. C. Swart and R. E. Kroon, *RSC Adv.*, 2023, **13**, 5353.

69 D. Napierska, I. Sanseverino, R. Loos, D. Marinov and T. Lettieri, *Review of the 1st Watch List under the Water Framework Directive and Recommendations for the 2nd Watch List*, Publications Office, 2018, DOI: 10.2760/614367.

70 G. Provinciali, G. Bicchierai, A. L. Capodilupo, A. Mauri, J. Fu, D. Liu, G. Giambastiani, G. Tuci, S. Galli, C. Piccirillo and A. Rossin, *J. Mater. Chem. C*, 2025, **13**, 16427.

71 G. Mercuri, M. Moroni, S. Galli, C. Piccirillo, A. L. Capodilupo, G. Tuci, G. Giambastiani and A. Rossin, *Inorg. Chem. Front.*, 2022, **9**, 90.